Appl. Phys. A (2016) 122:805
DOI 10.1007/s00339-016-0333-z

Applied Physics A
Materials Science & Processing

A novel unified dislocation density-based model for hot deformation behavior of a nickel-based superalloy under dynamic recrystallization conditions

Y. C. Lin[1,2,3] · Dong-Xu Wen[1] · Ming-Song Chen[1,3] · Xiao-Min Chen[1]

Received: 8 June 2016 / Accepted: 1 August 2016 / Published online: 9 August 2016

Abstract In this study, a novel unified dislocation density-based model is presented for characterizing hot deformation behaviors in a nickel-based superalloy under dynamic recrystallization (DRX) conditions. In the Kocks–Mecking model, a new softening item is proposed to represent the impacts of DRX behavior on dislocation density evolution. The grain size evolution and DRX kinetics are incorporated into the developed model. Material parameters of the developed model are calibrated by a derivative-free method of MATLAB software. Comparisons between experimental and predicted results confirm that the developed unified dislocation density-based model can nicely reproduce hot deformation behavior, DRX kinetics, and grain size evolution in wide scope of initial grain size, strain rate, and deformation temperature. Moreover, the developed unified dislocation density-based model is well employed to analyze the time-variant forming processes of the studied superalloy.

1 Introduction

In hot forming processes, metallic materials often undergo a series of plastic deformation (compression, tension, torsion, etc.) and heat treatments (tempering, annealing, normalization, etc.) [1]. Hot working parameters, including strain rate, strain, and deformation temperature, exert great impacts on hot deformation behavior in alloys. Meanwhile, the increase in stored energy caused by dislocation multiplication further results in the complicated microstructural evolution. Work hardening (WH), dynamic recovery (DRV), phase transformation, and dynamic recrystallization (DRX) often take place [2, 3] and affect hot deformation behaviors of metallic materials [4–6]. Therefore, a comprehensive investigation on the intrinsic interactions between microstructural evolution and hot deformation behavior is necessary [7, 8].

In recent years, numerous researchers have obtained some important insights in the microstructural evolution and hot deformation behavior of metals or alloys [9–11]. Based on the empirical observations, the phenomenological constitutive models (Arrhenius hyperbolic-sine equation, etc.) are often developed to characterize hot deformation behavior of metallic materials [12–17]. The ease to calibrate material parameters and the relatively high prediction accuracy facilitate wide use of phenomenological constitutive models under the experimental conditions. However, due to their empirical characteristics, the application scope of phenomenological constitutive models is limited and cannot be extrapolated to the wide scope of hot working parameters [1]. In contrast, some important theoretical advances in physical mechanism, such as dislocation density theory, thermodynamics, and crystal plasticity, make the physical-based constitutive models practicable [18–23]. Kocks–Mecking (KM) model is one widely applied approach to characterize hot deformation behavior of metallic materials, in which the dislocation density evolution is regarded as a competing process between dislocation generation and annihilation [19]. The average dislocation density is the single internal variable in KM

✉ Y. C. Lin
yclin@csu.edu.cn; linyongcheng@163.com

[1] School of Mechanical and Electrical Engineering, Central South University, Changsha 410083, China

[2] Light Alloy Research Institute of Central South University, Changsha 410083, China

[3] State Key Laboratory of High Performance Complex Manufacturing, Changsha 410083, China

model. Due to the insufficiency of one-internal-variable KM model for dislocation interactions, some suitable two-internal-variable and three-internal-variable models are proposed to account for the effects of dislocation cell, vacancy concentration, or precipitate hardening on dislocation density evolution [24–26].

Nickel-based superalloys with precipitation strengthening features are numerously employed in aviation and energy industries [27, 28]. The excellent mechanical properties mainly attribute to the high alloying element contents and advanced heat treatment methods. Both γ'' (Ni_3Nb) and γ' ($Ni_3(Al, Ti)$) precipitates are the main strengthening phases in nickel-based superalloys. However, γ'' precipitate is metastable and may transform to stable δ phase Ni_3Nb in equilibrium [29]. Due to the complex microstructures, the deformation mechanisms of nickel-based superalloy are very complicated. Several constitutive models [18, 30, 31] were established for characterizing the hot deformation behaviors for superalloys. Considering the comprehensive effects of hot working parameters and initial δ phase, Lin et al. [32] presented a novel phenomenological constitutive model for reproducing isothermal compression behaviors of GH4169 superalloy. Keshavarz and Ghosh [33] developed a crystal plasticity method for modeling nickel-based superalloy in terms of characteristics of γ–γ' microstructural morphology. Also, the microstructural evolution [34, 35], dynamic recrystallization behavior [36, 37], and grain boundaries characteristics [38] of some typical superalloys have been investigated.

Although numerous investigations on hot deformation behavior for some nickel-based superalloys have been conducted, the effects of dynamic recrystallization on dislocation density evolution and hot deformation behavior are still not clear. The models are still incapable to describe the physical mechanisms of hot deformation, as well as microstructural evolution. Especially, the previous constitutive models cannot be applied in time-variant condition. The object of this study is to develop a novel unified dislocation density-based approach for reproducing hot deformation and DRX behaviors in nickel-based superalloy. Also, the developed model can be employed to characterize the time-variant processes.

2 Experimental procedure

A nickel-based superalloy is selected for this investigation, and the chemical components (wt.%) is 52.82Ni–18.96Cr–5.23Nb–3.01Mo–1.00Ti–0.59Al–0.01Co–0.03C–(bal.)Fe. The studied superalloy is quite close to Inconel 718 alloy. Cylindrical samples (ϕ 8 × 12 mm) were machined from a wrought biscuit. Before the isothermal compressive experiments, the samples were heated up to 1313 K (1040 °C) for 45 min and then quenched by water to obtain the homogeneous microstructure. For analyzing the impacts of initial grain size on hot deformation behavior, three initial grain sizes (33, 48 and 75 μm) were obtained by suitable pretreatments. The isothermal compressive experiments were conducted by a Gleeble3500 thermo-mechanical simulator. For achieving an even temperature distribution before loading, the samples were heated to experiment temperatures at the speed of 10 K/s, and then soaked for 5 min. Four strain rates (1, 0.1, 0.01, and 0.001 s^{-1}) and five deformation temperatures (1313, 1283, 1253, 1223, and 1193 K), (1040, 1010, 980, 950, and 920 °C) were used. The deformation temperatures and strain rates were all selected from the practice industrial hot forming processes, such as harmer forging, conventional die forging, and isothermal die forging [39]. It is well known that the grain growth is very sensitive to the deformation temperature, and is hardly controlled for nickel-based superalloys. However, the rate of grain growth for the studied superalloy is slow in the selected deformation temperature range [40]. Therefore, only the initial grain size is determined before isothermal compressive experiments, and the grain growth during heating process is ignored. The samples were compressed to 30 % height and quenched by water. The nominal average true strain of the specimen reaches 1.2. During the isothermal compression, a closed loop control testing system is applied to execute the experimental procedures and record the experimental data.

3 Development of a novel unified dislocation density-based model

During hot deformation, the obvious WH, DRV, and DRX behaviors are found in nickel-based superalloys for the competition of dislocation multiplication and annihilation [41–43]. The WH and DRV behaviors can be well reproduced by the classical dislocation density theory, in which stress–strain relationship and microstructural state of materials are represented by dislocation density evolution [18]. For the studied superalloy, a typical low SFE metallic material, DRX is an important factor to induce dynamic softening and further significantly impacts dislocation density evolution during hot deformation [34]. The fine recrystallized grains affect the dislocation mean free path and enhance WH behavior. Meanwhile, the recombination of dislocation reduces the dislocation density during DRX. Meanwhile, the fine recrystallized grains facilitate the grain boundary sliding and promote the dynamic softening behavior. In order to comprehensively consider the impacts of WH, DRV, and DRX on hot deformation behavior, the

classical dislocation density theory should be further improved by incorporating the dynamic recrystallization mechanism.

During low-moderate temperature deformation (lower than the recrystallization temperature), it is commonly assumed that the true stress consists two parts, i.e., the short-range stress for the activation of dislocation slip (σ_y) and the stress caused by the dislocation substructure interactions (σ_i) [19]. Once the deformation temperature exceeds recrystallization temperature, dynamic recrystallization occurs, which accompanies the obvious dynamic softening. In present work, a stress item (σ_g) is developed to represent the impacts of grain size evolution on true stress.

$$\sigma = \sigma_y + \sigma_i + \sigma_g \tag{1}$$

The details in the developed model will be discussed in the following sections.

3.1 Evaluation of σ_y

During hot deformation, the dislocation mobility is determined by a thermally activated process. As the deformation temperature increased, dislocation climb gradually replaces dislocation cross-slip as the main characteristics of dislocation motion. The impacts of initial grain size, strain rate, and deformation temperature on the short-range stress (σ_y) for activating dislocation motion can be represented as an Arrhenius type relation. In authors' previous work [44], the values of short-range stresses at variant experiment conditions have been already obtained, and the relationships of short-range stress, initial grain size, strain rate, and deformation temperature are expressed as,

$$\sigma_{\mathrm{y}} = 0.708 d_0^{-0.123} \left(\dot{\varepsilon} \exp\left(\frac{663870}{\mathrm{RT}} \right) \right)^{0.09} \tag{2}$$

where T is deformation temperature, $\dot{\varepsilon}$ is strain rate, d_0 is initial grain size, and R is the universal gas constant (8.314 J mol^{-1} K^{-1}). The selected deformation temperature and strain rate in this study all conform the applicable range of this relationship.

3.2 Evaluation of σ_i

With the increase in externally applied loading, the plastic stage appears, once the yield limit is exceeded. In the plastic stage, the slip systems are activated, and the competitions between dislocation storage and annihilation result in the complicated variations in dislocation density, which further leads to the changed true stress during hot deformation. According to Kocks–Mecking model [18], the stress caused by the dislocation interactions (σ_i) is represented as,

$$\sigma_i = M \alpha \mu b \sqrt{\rho_i} \tag{3}$$

where ρ_i is average dislocation density. α is dislocation interaction constant and equals to 0.3 [24]. μ is shear modulus, and $\mu = 86.94–0.027\ T$ [45]. M is the Taylor factor correlating shear stress/shear strain to effective stress/plastic strain, which equals to 3.06 for FCC metallic materials [46]. b is Burgers vector (2.54×10^{-10} m for the studied superalloy) [30].

In Kocks–Mecking model [18], the dislocation density evolution is expressed as,

$$\dot{\rho}_i = \dot{\rho}_i^{+} - \dot{\rho}_{i(\mathrm{drv})}^{-} \tag{4}$$

where $\dot{\rho}_i^{+}$ is WH item, $\dot{\rho}_{i(\mathrm{drv})}^{-}$ is DRV item.

However, for the low SFE metallic material, such as nickel-based superalloy, dynamic recovery caused by dislocation cross-slip and climb proceeds slowly during hot deformation [34]. The high deformation stored energy promotes the occurrence of DRX, which is another important dynamic softening mechanism for the studied superalloy, and significantly impacts dislocation density evolution during hot deformation. Therefore, in present study, an additional softening item ($\dot{\rho}_{i(\mathrm{drx})}^{-}$) is proposed to represent the impacts of DRX on dislocation density evolution. Then, Eq. (4) can be updated as,

$$\dot{\rho}_i = \dot{\rho}_i^{+} - \dot{\rho}_{i(\mathrm{drv})}^{-} - \dot{\rho}_{i(\mathrm{drx})}^{-} \tag{5}$$

In the following sections, WH item ($\dot{\rho}_i^{+}$), DRV item ($\dot{\rho}_{i(\mathrm{drv})}^{-}$), as well as DRX item ($\dot{\rho}_{i(\mathrm{drx})}^{-}$) of the studied superalloy will be evaluated in detail, respectively.

3.2.1 Work hardening item $\dot{\rho}_i^{+}$

Before mobile dislocations meet impenetrable obstacles, the mean traveled distance is termed as dislocation mean free path (Λ). According to Orowan equation, the accumulation rate of dislocation density is inversely proportional to Λ, and proportional to strain rate ($\dot{\varepsilon}$). So, the accumulation rate of dislocation density during hot deformation is assumed as [22, 30],

$$\dot{\rho}_i^{+} = \frac{M}{b} \frac{1}{\Lambda} \dot{\varepsilon} \tag{6}$$

The mean free path (Λ) is highly relevant with the dislocation substructures, grain boundaries, precipitates, etc. In this study, the studied superalloy undergoes solution treatment before isothermal compression tests. The effects of precipitates on mean free path are ignored. So, the mean free path is assumed as summation of the inverses of substructure diameter (s_i) and average grain size (d_i) [22, 30].

$$\frac{1}{\Lambda} = \left(\frac{1}{s_i} + \frac{1}{d_i}\right) \tag{7}$$

Dislocation cell or substructure diameter (s_i) can be expressed as [22, 30],

$$s_i = \frac{f_w}{\sqrt{\rho_i}} \tag{8}$$

where f_w is the work hardening coefficient, which is dependent on initial deformation conditions.

During the initial deformation, WH and DRV are the main deformation mechanisms. Furthermore, the grain size can be assumed to be constant. With the further straining, the dynamic recrystallization appears, and the grains are obviously refined. Thus, the average grain size (d_i) is significantly affected by DRX volume fraction (X_i). So, the grain size evolution under DRX conditions can be expressed as,

$$d_i = X_i d_{drx} + (1 - X_i) d_0 \tag{9}$$

where d_0 and d_{drx} are initial and DRX grain sizes, respectively. X_i is DRX volume fraction.

Generally, the dynamic recrystallization behavior experiences an initial incubation, accelerating, and steady periods. According to Avrami equation, the DRX kinetics is described by [41, 47].

$$X_i = 1 - \exp\left(-\ln 2\left(\frac{\varepsilon - \varepsilon_c}{\varepsilon_{0.5} - \varepsilon_c}\right)^{f_d}\right) \quad \varepsilon \geq \varepsilon_c \tag{10}$$

where ε_c is the critical strain for initiating DRX, f_d is DRX exponent, and $\varepsilon_{0.5}$ is the strain for 50 % DRX volume fraction.

In authors' previous work [41], the dynamically recrystallized grain size (d_{drx}) had been directly evaluated from the experimental results by the linear intercept method. The relationships of DRX grain size, initial grain size, strain rate, and deformation temperature can be expressed as an Arrhenius type relation by Eq. (11). The detailed modeling procedures to develop this model are presented in "Appendix".

$$d_{drx} = 737.151 d_0^{0.329} \left(\dot{\varepsilon} \exp\left(\frac{474000}{RT}\right)\right)^{-0.139} \tag{11}$$

3.2.2 Dynamic recovery item $\dot{\rho}^{-}_{i(drv)}$

During dynamic recovery, there is a reduction in average dislocation density, as well as alteration in dislocation configuration, for metals or alloys [48]. At low-moderate temperatures, the most important step in dynamic recovery processes is widely thought to be cross-slip, which is validated by the appearance of wavy slip traces [49]. As the deformation temperature is increased, the vacancy movement becomes active and accelerates dislocation climb. At high deformation temperatures, dislocation climb becomes a potentially important dynamic recovery mechanism, accompanying an evident temperature and time dependence [48]. According to Kocks–Mecking model, the rate of DRV is proportional to dislocation density [24]. i.e.,

$$\dot{\rho}^{-}_{i(drv)} = f_v \rho_i \dot{\varepsilon} \tag{12}$$

where f_v is the dynamic recovery coefficient, which is dependent on initial deformation conditions.

3.2.3 Dynamic recrystallization item $\dot{\rho}^{-}_{i(drx)}$

Figure 1 shows the schematic of DRX process in the studied superalloy. During initial state, the microstructure mainly contains equiaxed grains with a low dislocation density. As plastic strain increases, the dislocation generation and multiplication take place. When dislocations encounter barriers (vacancy, dislocation, grain boundary, etc.), dislocation cross-slip or dislocation climb is difficult to proceed for the low SFE metallic material. The dislocation annihilation induced by DRV can hardly balance dislocation multiplication. High density dislocations are tangled and intersected. With the critical dislocation density arriving, the nucleation and growth of DRX grain takes place. The dislocation density in the dynamically recrystallized region decreases greatly, which can be assumed to be the same as the initial material. With the further straining, the degree of DRX gradually increases. Then, the effects of DRX on dislocation density evolution become more and more significant.

However, only the average dislocation density is applied in Kocks–Mecking model. In order to assess the dislocation density evolution in local dynamically recrystallized region, DRX volume fraction (X_i) should be considered. The dislocation density in new dynamically recrystallized grain ($\rho_{i(drx)}$) can be assumed to be equal to that in the initial material ($\rho_{i-i(cr)}$). The annihilation rate of dislocation density in the local dynamically recrystallized region ($\dot{\rho}_{i(drx)}$) is proportional to dislocation density in initial state ($\rho_{i-i(cr)}$). So, dislocation density evolution caused by DRX can be expressed as [49],

$$\dot{\rho}^{-}_{i(drx)} = X_i f_x \rho_{i-i(cr)} \dot{\varepsilon} \tag{13}$$

where f_x is the dynamic recrystallization coefficient, which is highly dependent on initial deformation conditions. Note that this item is active only when the critical dislocation density for dynamic recrystallization (ρ_{cr}) is exceeded.

In this study, both the critical strain and critical dislocation density are employed to represent the initiation of DRX (Eqs. 10 and 13). Based on the above analyses, the

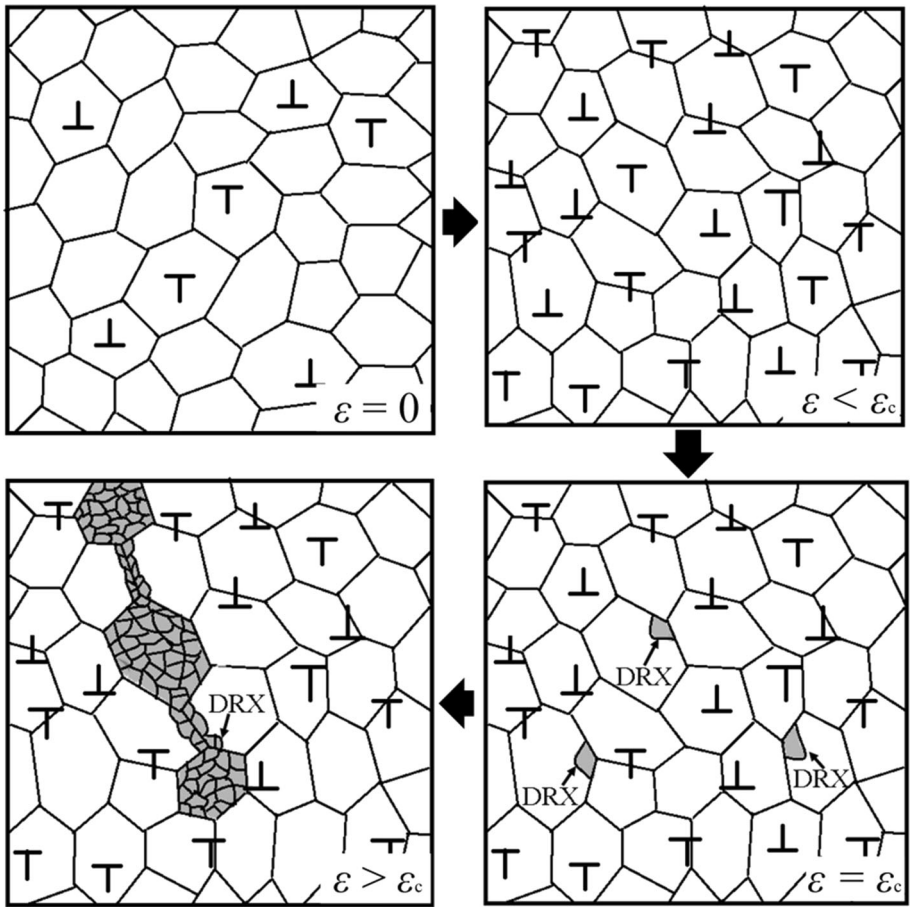

Fig. 1 Schematic of DRX process

dislocation density evolution is highly related to strain, and there is a one-to-one correspondence between dislocation density and strain. So, once the critical dislocation density is ascertained, the critical strain can be obtained. The critical dislocation density is evaluated by [50],

$$\rho_{cr} = \left(\frac{20s\dot{\varepsilon}}{3bLM_{bm}\lambda^2}\right)^{\frac{1}{3}} \tag{14}$$

where M_{bm} is grain boundary mobility. s is grain boundary energy, which is determined by the misorientations between two neighboring grains. λ is dislocation line energy, which is given by $\lambda = c\mu b^2$ (c is equal to 0.5). L is initial dislocation mean free path. For high-angle grain boundaries, s is directly obtained by [51],

$$s = \frac{\mu b\theta_m}{4\pi(1-\nu)} \tag{15}$$

where θ_m stands for the misorientation of high-angle grain boundary (15°). ν is the Poisson ratio and can be selected as 0.33 for present work.

The initial dislocation mean free path (L) is given by [52],

$$L = k_d b\left(\frac{\mu}{\sigma_y}\right)^m \tag{16}$$

where k_d and m are material constants and can be selected as 10 and 1.33, respectively [52].

The grain boundary mobility (M_{bm}) can be expressed as [52],

$$M_{bm} = \frac{b\delta D_{ob}}{k_b T}\exp\left(-\frac{Q_{dif}}{RT}\right) \tag{17}$$

where D_{ob} is grain boundary self-diffusion coefficient, and δ is the thickness of characteristic grain boundary. For the studied superalloy, δD_{ob} is equal to 3.5×10^{-15} m^3/s [53]. Q_{dif} is boundary diffusion activation energy (equal to 115 kJ/mol for the studied superalloy) [53]. k_b is the Boltzmann constant (1.381×10^{-23} J/K), and R is the universal gas constant.

3.3 Evaluation of σ_g

During hot deformation, the fine recrystallized grains can facilitate grain boundary sliding and boost dynamic softening behavior. So, metallic materials with fine grains always represent the low true stress during hot deformation. In this study, it is assumed that the impacts of fine recrystallized grains on true stresses can be represented by Eq. (18). i.e., the minus in Eq. (18) indicates that fine

recrystallized grains can induce the decease of the flow stress. Meanwhile, the dynamically recrystallized region should be considered.

$$\sigma_g = -X_i f_g d_i^{-1/2} \tag{18}$$

where X_i is DRX volume fraction. f_g is grain size evolution coefficient, which is dependent on initial experiment conditions. d_i is the average grain size.

4 Computational procedures

In order to implement the developed unified dislocation density-based model, several material parameters (WH coefficient f_w, DRV coefficient f_v, DRX exponent f_d, DRX coefficient f_x, and grain size evolution coefficient f_g) would be determined and calibrated. According to authors' previous work [44], the WH coefficient f_w and DRV coefficient f_v are determined by,

$$f_w = A_w d_0^{m_w} \left(\dot{\varepsilon} \exp\left(\frac{Q_w}{RT}\right)\right)^{n_w} \tag{19}$$

$$f_v = A_v d_0^{m_v} \left(\dot{\varepsilon} \exp\left(\frac{Q_v}{RT}\right)\right)^{n_v} \tag{20}$$

where A_w, A_v, m_w, m_v, n_w, n_v, Q_w, and Q_v are material constants. The subscripts w and v correspond to WH and DRV, respectively.

Similarly, the dynamic recrystallization coefficient (f_x), grain size evolution coefficient (f_g), and dynamic recrystallization exponent (f_d) are assumed to follow the parallel relationships with initial grain size, strain rate, and deformation temperature.

$$f_x = A_x d_0^{m_x} \left(\dot{\varepsilon} \exp\left(\frac{Q_x}{RT}\right)\right)^{n_x} \tag{21}$$

$$f_g = A_g d_0^{m_g} \left(\dot{\varepsilon} \exp\left(\frac{Q_g}{RT}\right)\right)^{n_g} \tag{22}$$

$$f_d = A_d d_0^{m_d} \left(\dot{\varepsilon} \exp\left(\frac{Q_d}{RT}\right)\right)^{n_d} \tag{23}$$

where A_x, A_g, A_d, m_x, m_g, m_d, n_x, n_g, n_d, Q_x, Q_g, and Q_d are material parameters.

Then, there are twenty material parameters in Eqs. (19)–(23). In the following section, the material parameter solution procedure will be discussed in detail.

Generally, the DRX and grain size evolution are ignored in the WH-DRV stage, and the average grain size is regarded to be constant. Combining Eqs. (4), (6), and (12), the evolution equation for dislocation density in the WH-DRV stage is represented by,

$$\dot{\rho}_i = \frac{M}{b}\left(\frac{\sqrt{\rho_i}}{f_w} + \frac{1}{d_0}\right)\dot{\varepsilon} - f_v \rho_i \dot{\varepsilon} \tag{24}$$

When dislocation density exceeds the critical value for DRX, the nucleation and growth of DRX grain takes place. Combining Eqs. (5), (6), (12), and (13), the evolution equation for dislocation density under DRV and DRX conditions can be summarized as,

$$\dot{\rho}_i = \frac{M}{b}\left(\frac{\sqrt{\rho_i}}{f_w} + \frac{1}{d_i}\right)\dot{\varepsilon} - f_v \rho_i \dot{\varepsilon} - X_i f_x \rho_{i-i(\mathrm{cr})}\dot{\varepsilon} \tag{25}$$

In order to extend the applicable scope of the developed unified dislocation density-based model, the iterative procedures are proposed, and material parameters can be updated in every strain increment. The initial dislocation density is set as 1×10^{11} m^{-2} for the studied superalloy [44]. Then, dislocation density evolution in a strain increment ($\Delta\varepsilon$) is given by,

$$\Delta\rho_i = \frac{M}{b}\left(\frac{\sqrt{\rho_i}}{f_w} + \frac{1}{d_0}\right)\Delta\varepsilon - f_v \rho_i \Delta\varepsilon \quad \rho_i < \rho_{cr} \tag{26}$$

$$\Delta\rho_i = \frac{M}{b}\left(\frac{\sqrt{\rho_i}}{f_w} + \frac{1}{d_i}\right)\Delta\varepsilon - f_v \rho_i \Delta\varepsilon - X_i f_x \rho_{i-i(\mathrm{cr})}\Delta\varepsilon \quad \rho_i \geq \rho_{cr} \tag{27}$$

The stress increment ($\Delta\sigma_i$) caused by dislocation evolution is given by,

$$\Delta\sigma_i = \frac{\mathrm{d}\sigma_i}{\mathrm{d}\rho_i}\Delta\rho_i = \left(\frac{1}{2}\alpha M \mu b \rho_i^{-1/2}\right)\Delta\rho_i \tag{28}$$

The stress increment ($\Delta\sigma_g$) induced by grain size evolution can be expressed as,

$$\begin{aligned}\Delta\sigma_g &= \left(\frac{\partial\sigma_g}{\partial X_i}\frac{\partial X_i}{\partial\varepsilon} + \frac{\partial\sigma_g}{\partial d_i}\frac{\partial d_i}{\partial\varepsilon}\right)\Delta\varepsilon \\ &= -f_g d_i^{-1/2}\frac{\mathrm{d}X_i}{\mathrm{d}\varepsilon}\Delta\varepsilon + \frac{1}{2}X_i f_g d_i^{-3/2}\frac{\partial\vec{d}_i}{\partial\varepsilon}\Delta\varepsilon\end{aligned} \tag{29}$$

The difference forms of grain size evolution equation and DRX kinetic equation (Eqs. 9 and 10) are given by,

$$\Delta X_i = \ln 2 \frac{f_d}{\varepsilon_{0.5}}\left(\frac{\varepsilon - \varepsilon_c}{\varepsilon_{0.5} - \varepsilon_c}\right)^{f_d - 1} \exp\left(-\ln 2\left(\frac{\varepsilon - \varepsilon_c}{\varepsilon_{0.5} - \varepsilon_c}\right)^{f_d}\right)\Delta\varepsilon \tag{30}$$

$$\Delta d_i = -(d_0 - d_{\mathrm{drx}})\Delta X_i \tag{31}$$

From Eqs. (28–31), the stress increment in DRX period can be summarized as,

$$\begin{aligned}\Delta\sigma &= \Delta\sigma_i + \Delta\sigma_g \\ &= \left(\frac{1}{2}\alpha M \mu b \rho_i^{-1/2}\right)\Delta\rho_i \\ &\quad - f_g\left(1 + \frac{1}{2}X_i(\mathrm{d}_0 - \mathrm{d}_{\mathrm{drx}})\Big/\mathrm{d}_i\right)\mathrm{d}_i^{-1/2}\Delta X_i\end{aligned} \tag{32}$$

The critical dislocation density can be directly evaluated by Eqs. (14)–(17). Due to a one-to-one correspondence between strain and dislocation density, the critical strain can be easily determined by integrating Eq. (26),

$$\rho_{\mathrm{cr}} = \int_0^{\varepsilon_c} \dot{\rho}_i \mathrm{d}\varepsilon = \int_0^{\varepsilon_c} \left(\frac{M}{b} \left(\frac{\sqrt{\rho_i}}{f_{\mathrm{w}}} + \frac{1}{d_0} \right) - f_{\mathrm{v}} \rho_i \right) \mathrm{d}\varepsilon \tag{33}$$

The strain for 50 % DRX volume fraction ($\varepsilon_{0.5}$) is another key in the developed model. Generally, the DRX volume fraction (X_i) also can be evaluated by [41].

$$X_i = \frac{\sigma_{\mathrm{rec}} - \sigma}{\sigma_{\mathrm{sat}} - \sigma_{\mathrm{ss}}} \tag{34}$$

where σ_{rec} is recovery stress, σ is predicted true stress, σ_{sat} is saturation stress, andσ_{ss} is steady stress.

The recovery stress (σ_{rec}) is obtained under the condition that DRX is unavailable, and the main deformation mechanism is WH and DRV. So, the recovery stress (σ_{rec}) can be directly determined by Eqs. (1), (2), (3), and (26). If the balance between WH and DRV is obtained, the accumulation rate of dislocation density approaches zero, then the saturation stress (σ_{sat}) appears. Combining Eqs. (1), (2), (3), and (24), the saturation stress (σ_{sat}) can be expressed as,

$$\sigma_{\mathrm{sat}} = \lim_{\varepsilon \to \infty} \sigma_{\mathrm{rec}} = \sigma_y + \frac{M\alpha\mu b}{2f_{\mathrm{v}}} \left(\frac{M}{bf_{\mathrm{w}}} + \sqrt{\left(\frac{M}{bf_{\mathrm{w}}} \right)^2 + \frac{4f_{\mathrm{v}}M}{bd_0}} \right) \tag{35}$$

Then, the DRX takes place with the critical dislocation density arriving. The DRX degree quickly increases with further straining. When the balance between WH, DRV, and DRX is reached, the flow stress (σ) gradually reaches to a steady state (σ_{ss}). Combining Eqs. (1), (2), (3), (18), and (25), the steady stress (σ_{ss}) can be expressed as,

$$\begin{aligned} \sigma_{\mathrm{ss}} &= \lim_{\varepsilon \to \infty} \sigma \\ &= \sigma_y + \frac{M\alpha\mu b}{2(f_{\mathrm{v}} + f_{\mathrm{x}})} \left(\frac{M}{bf_{\mathrm{w}}} + \sqrt{\left(\frac{M}{bf_{\mathrm{w}}} \right)^2 + \frac{4(f_{\mathrm{v}} + f_{\mathrm{x}})M}{bd_{\mathrm{drx}}}} \right) \\ &\quad - \frac{f_{\mathrm{g}}}{\sqrt{d_{\mathrm{drx}}}} \end{aligned} \tag{36}$$

Substituting Eqs. (35–36) into Eq. (34), the strain for 50 % DRX volume fraction ($\varepsilon_{0.5}$) is determined by the iterative procedure.

In this investigation, the established state evolution equations are programmed in MATLAB software by utilizing implicit iterative procedures. Twenty material parameters (A_{w}, A_{v}, A_{x}, A_{g}, A_{d}, m_{w}, m_{v}, m_{x}, m_{g}, m_{d}, n_{w}, n_{v}, n_{x}, n_{g}, n_{d}, Q_{w}, Q_{v}, Q_{x}, Q_{g}, and Q_{d}) are optimized and calibrated by a derivative-free method in MATLAB toolbox. Figure 2 illustrates the algorithmic idea and flow chart of the developed unified dislocation density-based model. A group of initial values of material parameters need to be input into the program for trial. In the first iterative loop, the critical strain for initiating DRX (ε_c) is determined by comparing the predicted dislocation density with the critical dislocation density in theory. By substituting the critical strain and initial values of material parameters into the second iterative loop, the strain ($\varepsilon_{0.5}$) for 50 % DRX volume fraction is obtained. The material parameters in the developed model are all determined, and the predicted true stress (σ) can be obtained. By comparing the predicted (σ) and experimental true stresses (σ_m), the initial values of material parameters can be optimized by derivative-free method again and again. When the output of material parameter tolerance or the function tolerance is lower than 10^{-4}, the optimization process is stop, and a group of optimal material parameters can be obtained. Then, the developed model is determined. The optimal material parameters are presented in Table 1.

5 Discussion

In Sect. 4, all the necessary material parameters are calibrated and determined. Substituting the material parameters into the program developed by MATLAB software, the hot deformation behavior and dynamic recrystallization kinetics in the studied superalloy are easily reproduced.

Figures 3, 4, and 5 show the experimental and predicted flow stress curves at all experimental conditions. The predicted flow stress curves start from the short-range stress (σ_y). The predicted true stresses (σ) nicely coincide with the measured data (σ_m). So, the developed unified dislocation density-based model well characterizes the hot deformation behaviors in the studied superalloy. In Figs. 3, 4, and 5, it can be found that the dynamic softening behavior proceeds fast with the initial grain size decreasing. Based on authors' previous study [38], discontinuous dynamic recrystallization (DDRX) is the dominant dynamic recrystallization mechanism for the studied superalloy. New grains preferentially nucleate on the original grain boundaries for discontinuous dynamic recrystallization. The initial microstructure with fine grains provides numerous nucleation sites and further promotes the progress of DRX, compared to that with coarse grains. Therefore, the dynamic softening behavior proceeds fast for the studied superalloy with the decrease of initial grain size.

Figures 6, 7, and 8 show the variations in the predicted DRX volume fraction (X_i) and average grain size with true strain under all experiment conditions. The DRX volume fraction is dramatically influenced by initial grain size, true strain, deformation temperature, and strain rate. The

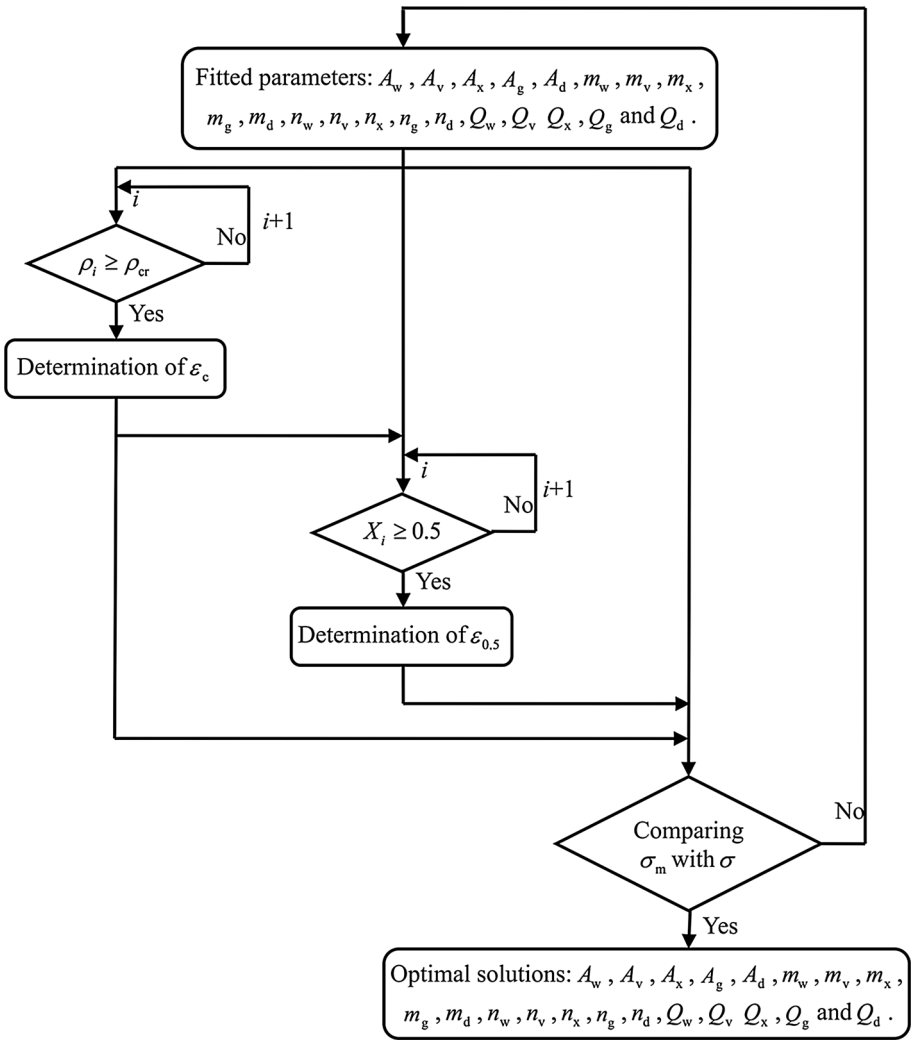

Fig. 2 Algorithmic idea and flow chart

Table 1 Optimized values of material parameters

Material parameters	Values	Material parameters	Values
A_w	1.092×10^4	n_x	−0.028
m_w	0.316	Q_x (kJ/mol)	1394.140
n_w	−0.160	A_g	1.169×10^{-4}
Q_w (kJ/mol)	455.296	m_g	−0.622
A_v	1.307×10^5	n_g	0.081
m_v	−1.211	Q_g (kJ/mol)	1236.647
n_v	−0.108	A_d	1.261×10^5
Q_v (kJ/mol)	467.553	m_d	0.036
A_x	2526.560	n_d	−0.029
m_x	−0.266	Q_d (kJ/mol)	4227.075

variation trend in DRX volume fraction with true strain well coincides with the basic hot deformation mechanisms. Under fine initial grain sizes, low strain rates or high deformation temperatures, the hot deformation behavior easily reaches to steady state. It is indicated that the dynamic recrystallization proceeds quickly, and the complete dynamic recrystallization easily occurs. Under fine initial grain size, high deformation temperature or low strain rate, dynamic recrystallization proceeds quickly, and then the corresponding average grain size easily reaches the steady state. However, the average grain size decreases continuously due to the incomplete dynamic

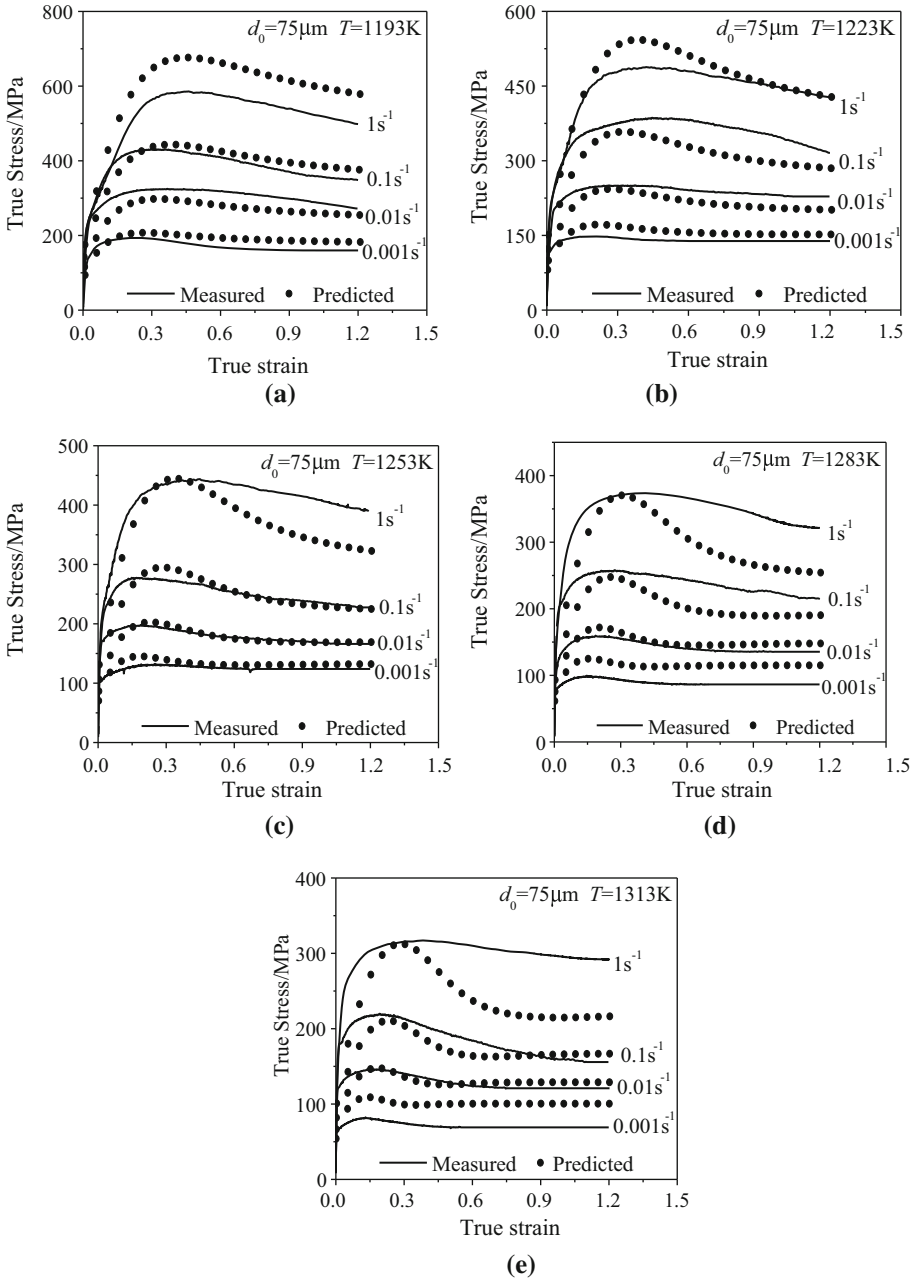

Fig. 3 Predicted and experimental true stresses at the initial grain size of 75 μm and deformation temperatures of: **a** 1193 K (920 °C); **b** 1223 K (950 °C); **c** 1253 K (980 °C); **d** 1283 K (1010 °C); **e** 1313 K (1040 °C)

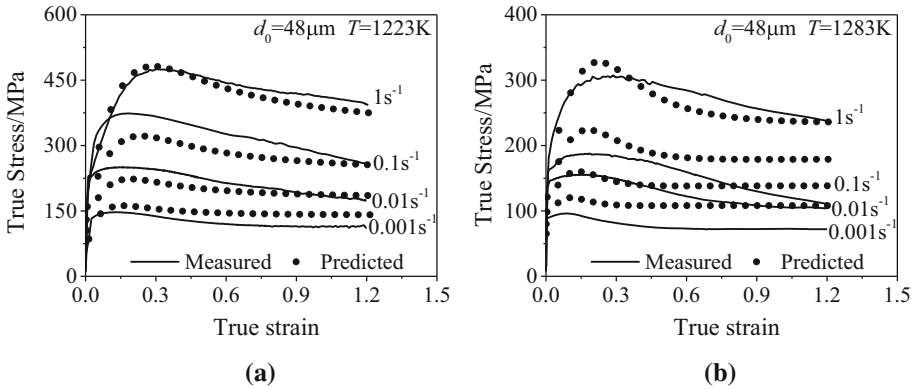

Fig. 4 Predicted and experimental true stresses at the initial grain size of 48 μm and deformation temperatures of: **a** 1223 K (950 °C); **b** 1283 K (1010 °C)

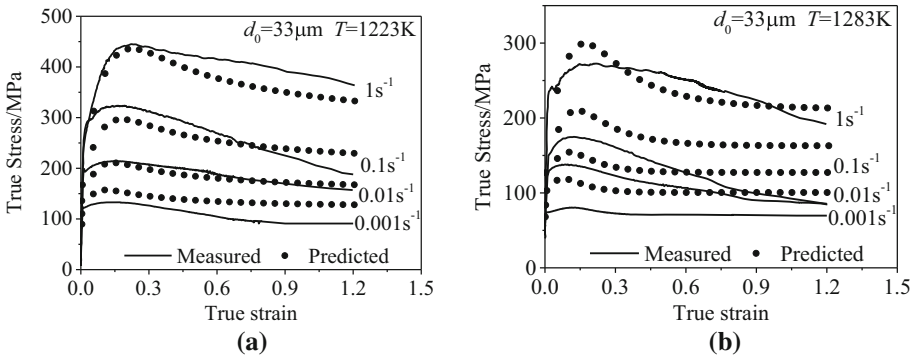

Fig. 5 Predicted and experimental true stresses at the initial grain size of 33 μm and deformation temperatures of: **a** 1223 K (950 °C); **b** 1283 K (1010 °C)

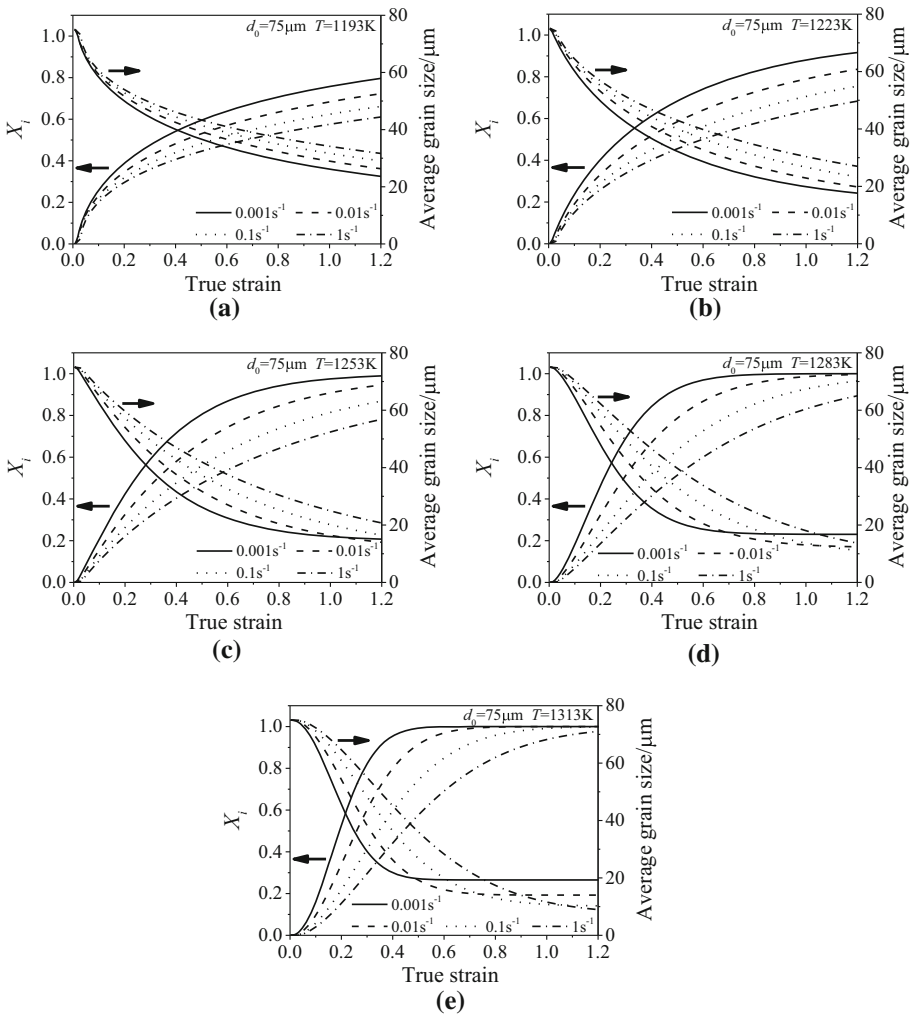

Fig. 6 Variations of DRX volume fraction and average grain size with true strain at the initial grain size of 75 μm and deformation temperatures of: **a** 1193 K (920 °C); **b** 1223 K (950 °C); **c** 1253 K (980 °C); **d** 1283 K (1010 °C); **e** 1313 K (1040 °C)

recrystallization at high strain rate/low deformation temperature. Under full dynamic recrystallization conditions, the averaged grain size decreases with decreasing deformation temperature or increasing strain rate.

The deformed microstructure of the studied superalloy is observed and quantitatively evaluated for assessing the accuracy of the developed unified dislocation density-based model. Figure 9 shows the typical deformed microstructures at the tested deformation temperatures and strain rates. The true strain of the deformated specimen reaches 1.2, and the initial grain size of the deformed microstructures is 75 μm. From Fig. 9, it is easily detected that DRX behavior of the studied superalloy highly related to deformation parameters. The DRX degree and DRX grain size significantly increase with decreasing strain rates or increasing deformation temperatures. On the one hand, as a thermally activated process, DRX occurs slowly at low deformation temperatures due to the insufficient energy for

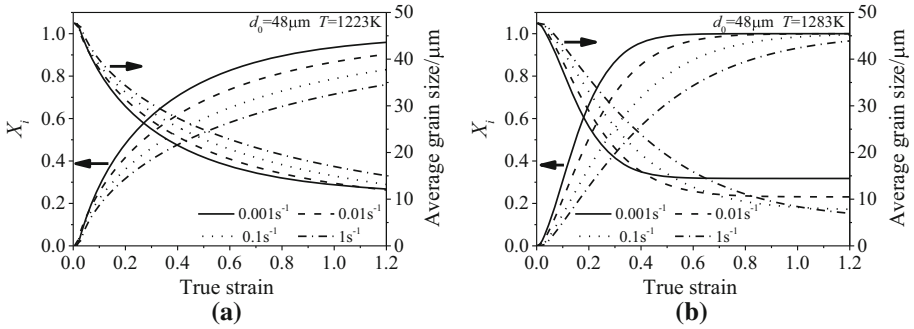

Fig. 7 Variations of DRX volume fraction and average grain size with true strain at the initial grain size of 48 μm and deformation temperatures of: **a** 1223 K (950 °C); **b** 1283 K (1010 °C)

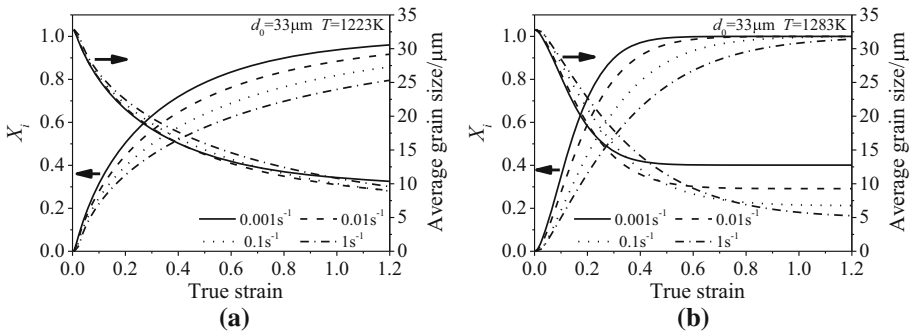

Fig. 8 Variations of DRX volume fraction and average grain size with true strain at the initial grain size of 33 μm and deformation temperatures of: **a** 1223 K (950 °C); **b** 1283 K (1010 °C)

grain boundary migration. However, the deformation period is too short at high strain rates, and the nucleation and growth of DRX grain hardly takes place. This well coincides with the predictions by the developed unified dislocation density-based model, as shown in Figs. 6, 7, and 8. Also, it can be found from Fig. 9 that there are some large grains. The main reason for this phenomenon is that the samples were compressed with the deformation degree of 70 %. Some original gains would be significantly elongated perpendicular to the compression direction. Therefore, some elongated gains seem so large, and even larger than the initial ones.

For further validating the developed unified dislocation density-based model, the correlation coefficient (R) between the predicted and experimental results is calculated.

$$R = \frac{\sum_{i=1}^{N}(E_i - \bar{E})(P_i - \bar{P})}{\sqrt{\sum_{i=1}^{N}(E_i - \bar{E})^2 \sum_{i=1}^{N}(P_i - \bar{P})^2}} \tag{37}$$

where E_i is the experimental values. P_i is the predicted values. N is the amount of samples. $\bar{E}$ is the mean value of E_i. $\bar{P}$ is the mean value of P_i.

The comparisons between predicted and experimental true stresses at all the experiment conditions are shown in Fig. 10. The correlation coefficient between predicted and experimental true stresses reaches to 0.965. Moreover, the majority of the predicted results are closely within ±50 MPa. Figure 11 shows the comparisons between the predicted and experimental DRX volume fractions at true strain of 1.2. The correlation coefficient between the predicted and experimental DRX volume fractions is 0.908. Thus, it is easily concluded from the above analyses that the developed unified dislocation density-based model has an excellent capability to reproduce WH, DRV, and DRX behaviors in the studied superalloy over wide scope of initial grain size, strain rate, and deformation temperature.

In industrial hot forming processes, the variations in deformation temperature and strain rate are inevitable due to the switch of processing routes. However, seldom constitutive models are capable of characterizing the hot deformation behavior at time-variant conditions, especially for the case with the complicated microstructural evolution. However, in this study, the developed unified dislocation density-based model can be successfully applied for describing the hot deformation and DRX behaviors at the time-variant conditions. Strain rate or deformation temperature can be freely updated in every strain increment by the designed iterative procedures during the whole hot forming. Meanwhile, the material parameters (short-range stress σ_y, WH coefficient f_w, DRV coefficient f_v, DRX exponent f_d, DRX coefficient f_x, and grain size evolution coefficient f_g, etc.) can also be updated in every strain increment. In order to further illustrate this point, time-variant isothermal compression tests are conducted. Two loading routes are given at deformation temperature of 1253 K (980 °C), and the experimental true stress is shown in Figs. 12 and 13. In the first loading route, strain rate is suddenly changed from 0.001 to 0.1 s^{-1} at the strain of 0.35 (Fig. 12a). The opposite change of strain rate is

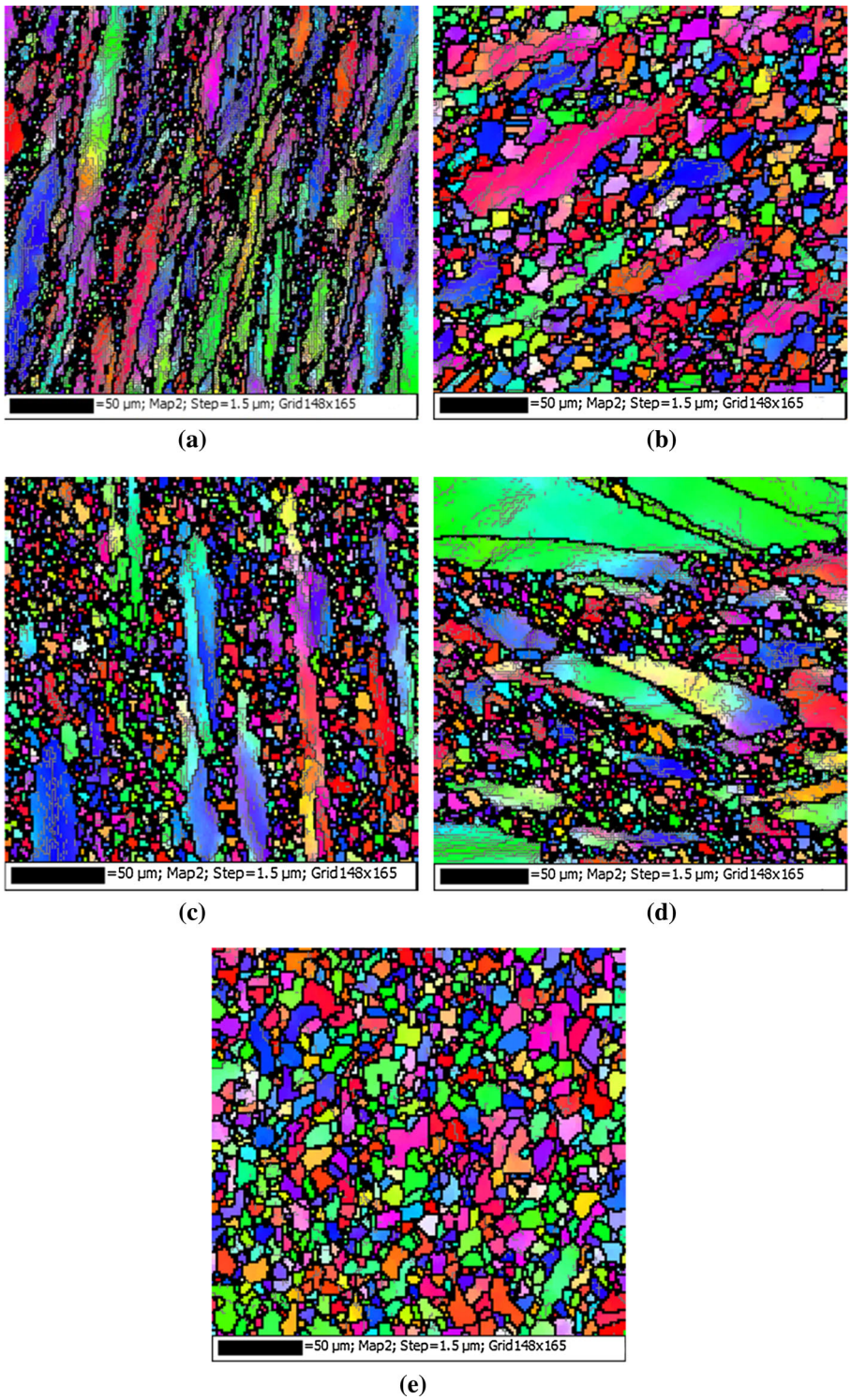

Fig. 9 Deformed microstructures of the studied superalloy at: **a** 1193 K (920 °C) 0.01 s^{-1}; **b** 1253 K (980 °C) 0.001 s^{-1}; **c** 1253 K (980 °C) 0.01 s^{-1}; **d** 1253 K (980 °C) 0.1 s^{-1}; **e** 1313 K (1040 °C) 0.01 s^{-1}

presented in the second loading route (Fig. 13a). It can be easily detected from Figs. 12a and 13a that the predicted true stresses nicely coincide with the experimental data. When true strains exceed the abrupt points, the preset strain rates are suddenly updated as the new strain rate, and the corresponding material parameters are also updated. Meanwhile, the deformed microstructure in the former loading processing (composed of original grain and dynamically recrystallized grain or one of them) is served as the initial microstructure in the subsequent loading processing.

The corresponding variations of DRX volume fraction and average grain size with strain in both loading cases are presented in Figs. 12b and 13b. The DRX volume fraction

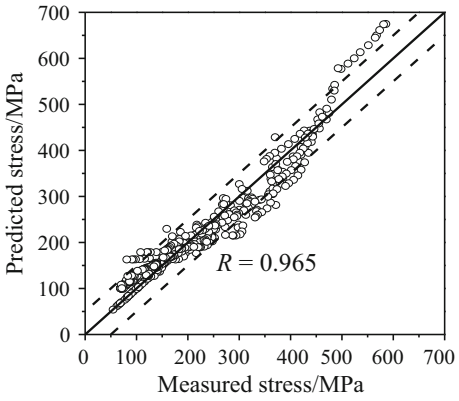

Fig. 10 Comparisons between the predicted and experimental true stresses (*Dash lines* indicate deviations of ±50 MPa)

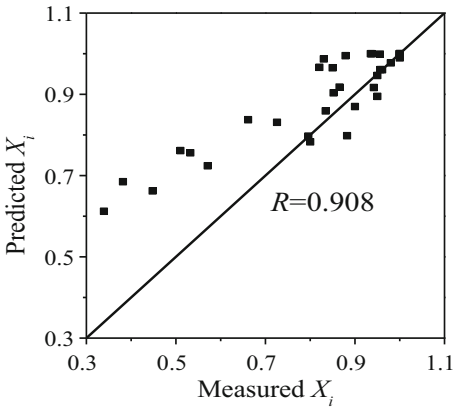

Fig. 11 Comparisons between the measured and predicted DRX volume fractions at the true strain of 1.2

can be determined by the iterative procedures of the Avrami model in difference form (Eq. 30). From Fig. 12b, it is easily detected that DRX volume fraction is almost approximate to 0.7 in the ending of the first stage. When strain rate is changed from 0.001 to 0.1 s^{-1}, the rate of dislocation multiplication rapidly increases, resulting in the increased true stress (Fig. 12a). When dislocation density exceeds the critical value for DRX at the new experiment condition, the dynamic recrystallization takes place. The deformed microstructures obtained from the first stage are recorded as the initial state of the second stage. So, the DRX volume fraction restarts from zero in the second stage. Figure 13b shows that the DRX volume fraction is less than 0.5 in the ending of the first stage. When strain rate is changed from 0.1 to 0.001 s^{-1}, the dynamic recrystallization proceeds quickly. This is because the high stored strain energy plays as the main driving force for DRX in the high strain rate stage. Therefore, DRX proceeds quickly when strain rate is rapidly decreased. With the further straining, the DRX volume fraction is almost approximate to 1, and the full dynamic recrystallization occurs. Then, the dynamic balance between WH, DRV, and DRX is obtained. Due to interactions between the microstructural evolution and hot deformation behavior, the variation of average grain size with true strain is very complicated, and the grain size evolution can be determined by Eqs. (30–31). The grain size evolutions corresponding to two loading routes are presented in Figs. 12b and 13b, respectively.

6 Conclusions

The hot deformation behavior in a nickel-based superalloy under dynamic recrystallization conditions is investigated by isothermal compressive experiments in the wide scope of initial grain size, strain rate, and deformation temperature. In order to comprehensively consider the impacts of WH, DRV, and DRX on hot deformation behavior, the dynamic recrystallization mechanism is introduced into the dislocation density theory. A novel physically based model is presented for characterizing hot deformation and dynamic recrystallization behaviors. The synthetic impacts of fine recrystallized grains on work hardening and dynamic softening are well settled. Synthesizing the coupled impacts of hot working parameters on hot deformation behaviors, short-range stress, dynamically recrystallized grain size, and several material parameters are determined by functions of initial grain size, strain rate, and deformation temperature. For characterizing the time-variant conditions, the implicit iterative procedures

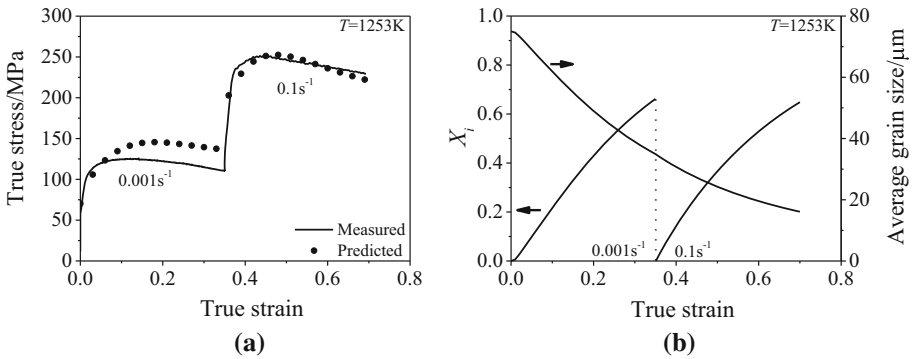

Fig. 12 Evolutions of: **a** true stress; **b** DRX volume fraction and average grain size (strain rate abruptly increased from 0.001 to 0.1 s^{-1} at the true strain of 0.35)

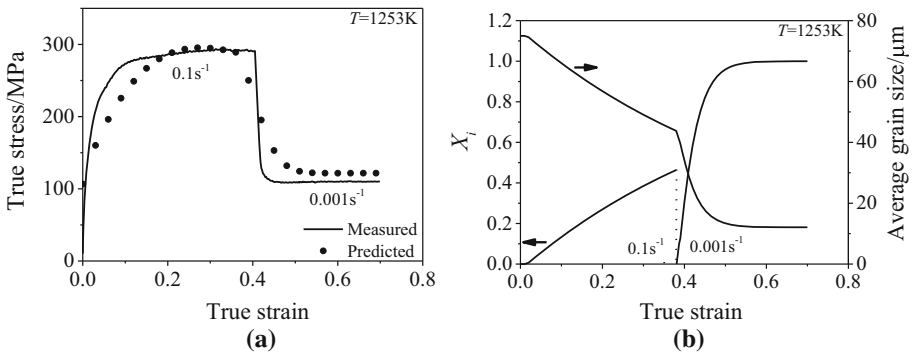

Fig. 13 Evolutions of: **a** true stress; **b** DRX volume fraction and average grain size (strain rate abruptly decreased from 0.1 to 0.001 s^{-1} at the true strain of 0.35)

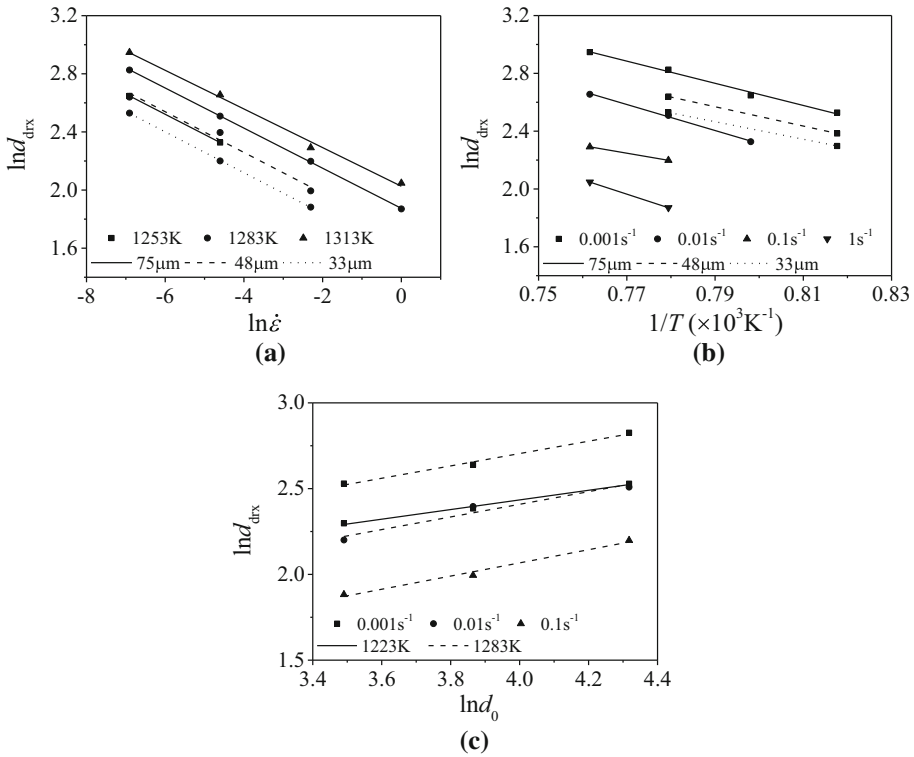

Fig. 14 Relationships of: **a** $\ln d_{drx} - \ln \dot{\varepsilon}$; **b** $\ln d_{drx} - 1/T$; **c** $\ln d_{drx} - \ln d_0$

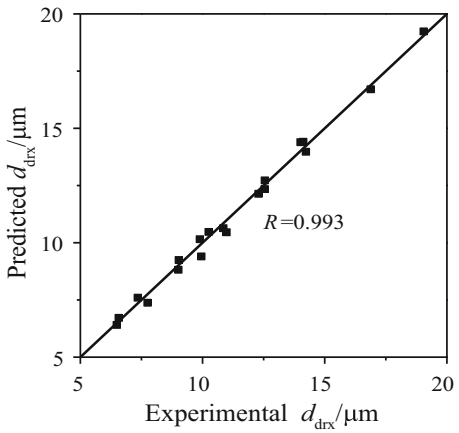

Fig. 15 Comparison between the predicted and experimental DRX grain sizes

are proposed in the developed model, which allows the updates of temperature and strain rate in every strain increment. The nice agreements between the predicted and experimental results confirm that the developed model is capable to characterize hot deformation and dynamic recrystallization behaviors. Moreover, the developed unified dislocation density-based model is well applied in the time-variant processes.

Acknowledgments This work was supported by the National Natural Science Foundation Council of China (Grant No. 51375502), the National Key Basic Research Program (Grant No. 2013CB035801), the Project of Innovation-driven Plan in Central South University (No. 2016CX008), the Natural Science Foundation for Distinguished Young Scholars of Hunan Province (Grant No. 2016JJ1017), and Hunan Provincial Innovation Foundation for Postgraduate (Grant No. CX2016B044).

Appendix

According to previous literatures [41], the DRX grain size is not only highly related to hot deformation parameters (strain rate, strain, and deformation temperature), but also to initial grain size. Thus, it is assumed that DRX grain size is represented as functions of deformation temperature, strain rate, as well as initial grain size [54],

$$d_{\mathrm{drx}} = A_r d_0^{m_r} \left(\dot{\varepsilon} \exp\left(\frac{Q_{\mathrm{r}}}{RT} \right) \right)^{n_{\mathrm{r}}} \tag{38}$$

where Q_r is experimental activation energy. A_{r}, m_{r}, and n_{r} are material constants.

The values of DRX grain size (d_{drx}) had been directly evaluated from the metallographic observations by the linear intercept method at selected experiment conditions. Substituting the experimental data into Eq. (37), the values of material parameters A_{r}, m_{r}, n_{r} and Q_{r} can be determined by $\ln d_{\mathrm{drx}} - \ln \dot{\varepsilon}$, $\ln d_{\mathrm{drx}} - 1/T$, and $\ln d_{\mathrm{drx}} - \ln d_0$ plots, as shown in Fig. 14. Then, the averaged values of A_{d}, m_{d}, n_{d}, and Q_{d} are calculated as 737.151, 0.329, −0.139, and 474,000 J/mol, respectively. Therefore, the model for DRX grain size is expressed as,

$$d_{\mathrm{drx}} = 737.151 d_0^{0.329} \left(\dot{\varepsilon} \exp\left(\frac{474000}{RT} \right) \right)^{-0.139} \tag{39}$$

The comparisons between the predicted and experimental DRX grain sizes are shown in Fig. 15. The correlation coefficient is 0.993, which confirms that the presented model can precisely reproduce the DRX grain size during hot deformation.

References

1. Y.C. Lin, X.M. Chen, Mater. Des. **32**, 1733 (2011)
2. Y.C. Lin, D.G. He, M.S. Chen, X.M. Chen, C.Y. Zhao, X. Ma, Z.L. Long, Mater. Des. **97**, 13 (2016)
3. L. Chen, G.Q. Zhao, J. Gong, X.X. Chen, M.M. Chen, J. Mater. Eng. Perform. **24**, 5002 (2015)
4. N. Nayan, G. Singh, S.V.S.N. Murty, A.K. Jha, B. Pant, K.M. George, U. Ramamurty, Intermetallics **55**, 145 (2014)
5. J. Yoon, S. Park, Mater. Des. **55**, 300 (2014)
6. R. Bobbili, V. Madhu, J. Mater. Eng. Perform. **24**, 4728 (2015)
7. Y.C. Lin, X.M. Chen, M.S. Chen, Y. Zhou, D.X. Wen, D.G. He, Appl. Phys. A **122**, 601 (2016)
8. F.C. Qin, Y.T. Li, H.P. Qi, L. Ju, J. Mater. Eng. Perform. **25**, 1237 (2016)
9. R. Bobbili, A. Paman, V. Madhu, Mater. Sci. Eng. A **651**, 753 (2016)
10. D. Samantaray, S. Mandal, C. Phaniraj, A.K. Bhaduri, Mater. Sci. Eng. A **528**, 8565 (2011)
11. A. Momeni, K. Dehghani, G.R. Ebrahimi, S. Kazemi, Metall. Mater. Trans. A **44**, 5567 (2013)
12. X.W. Yang, W.Y. Li, Metall. Mater. Trans. A **46**, 6052 (2015)
13. S.A.S. Vanini, M. Abolghasemzadeh, A. Assadi, Metall. Mater. Trans. A **44**, 3376 (2013)
14. Y.C. Lin, C.Y. Zhao, M.S. Chen, D.D. Chen, Appl. Phys. A **122**, 716 (2016)
15. A. Mirzaei, A. Zarei-Hanzaki, N. Haghdadi, A. Marandi, Mater. Sci. Eng. A **589**, 76 (2013)
16. E. Farabi, A. Zarei-Hanzaki, H.R. Abedi, J. Mater. Eng. Perform. **24**, 209 (2015)
17. J.Q. Tan, M. Zhan, S. Liu, T. Huang, J. Guo, H. Yang, Mater. Sci. Eng. A **631**, 214 (2015)
18. Y.C. Lin, X.M. Chen, D.X. Wen, M.S. Chen, Comput. Mater. Sci. **83**, 282 (2014)
19. H. Mecking, U.F. Kocks, Acta Metall. **29**, 1865 (1981)
20. A. He, G.L. Xie, X.Y. Yang, X.T. Wang, H.L. Zhang, Comput. Mater. Sci. **98**, 64 (2015)
21. Y.C. Lin, M.S. Chen, J. Zhong, Mech. Res. Commun. **35**, 142 (2008)
22. Y.C. Lin, D.X. Wen, M.S. Chen, Y.X. Liu, X.M. Chen, X. Ma, J. Mater. Res. (2016). doi:10.1557/jmr.2016.220
23. Y.Q. Ning, T. Wang, M.W. Fu, M.Z. Li, L. Wang, C.D. Zhao, Mater. Sci. Eng. A **642**, 187 (2015)
24. Y. Estrin, L.S. Tóth, A. Molinari, Y. Bréchet, Acta Mater. **46**, 5509 (1998)
25. F. Roters, D. Raabe, G. Gottstein, Acta Mater. **48**, 4181 (2000)
26. B. Babu, L. Lindgren, Int. J. Plast. **50**, 94 (2013)
27. M.S. Chen, Y.C. Lin, K.K. Li, Y. Zhou, Comput. Mater. Sci. **122**, 150 (2016)
28. J. Repper, P. Link, M. Hofmann, C. Krempaszky, W. Petry, E. Werner. Appl. Phys. A **99**, 565 (2010)
29. D.X. Wen, Y.C. Lin, J. Chen, X.M. Chen, J.L. Zhang, Y.J. Liang, L.T. Li, J. Alloys Compd. **618**, 372 (2015)
30. M. Fisk, J.C. Ion, L.E. Lindgren, Comput. Mater. Sci. **82**, 531 (2014)
31. A. Etaati, K. Dehghani, Mater. Chem. Phys. **140**, 208 (2013)
32. Y.C. Lin, M. He, M. Zhou, D.X. Wen, J. Chen, J. Mater. Eng. Perform. **24**, 3527 (2015)
33. S. Keshavarz, S. Ghosh, Acta Mater. **61**, 6549 (2013)
34. F. Chen, J. Liu, H. Ou, B. Lu, Z.S. Cui, H. Long, Mater. Sci. Eng. A **642**, 279 (2015)
35. D.X. Wen, Y.C. Lin, J. Chen, J. Deng, X.M. Chen, J.L. Zhang, M. He, Mater. Sci. Eng. A **620**, 319 (2015)
36. Y.X. Liu, Y.C. Lin, H.B. Li, D.X. Wen, X.M. Chen, M.S. Chen, Mater. Sci. Eng. A **626**, 432 (2015)
37. F. Tancret, E.I. Galindo-Nava, P.E.J. Rivera-Díaz-del-Castillo, Mater. Des. **103**, 293 (2016)
38. Y.C. Lin, X.Y. Wu, X.M. Chen, J. Chen, D.X. Wen, J.L. Zhang, L.T. Li, J. Alloys Compd. **640**, 101 (2015)
39. D.X. Wen, Y.C. Lin, H.B. Li, X.M. Chen, J. Deng, L.T. Li, Mater. Sci. Eng. A **591**, 183 (2014)
40. A. Kermanpur, W. Wang, P.D. Lee, M. McLean, Mater. Sci. Technol. **19**, 859 (2003)
41. X.M. Chen, Y.C. Lin, D.X. Wen, J.L. Zhang, M. He, Mater. Des. **57**, 568 (2014)
42. H.Q. Liang, H.Z. Guo, K. Tan, Y.Q. Ning, X. Luo, G. Cao, J.J. Wang, P.L. Zhen, Mater. Sci. Eng. A **638**, 357 (2015)
43. P.M. Souza, H. Beladi, R. Singh, B. Rolfe, P.D. Hodgson, Mater. Sci. Eng. A **648**, 265 (2015)
44. Y.C. Lin, D.X. Wen, Y.C. Huang, X.M. Chen, X.W. Chen, J. Mater. Res. **30**, 3784 (2015)
45. M. Fukuhara, A. Sanpei, J. Mater. Sci. Lett. **12**, 1122 (1993)
46. H. Mecking, U.F. Kocks, C. Hartig, Scr. Mater. **35**, 465 (1996)
47. F. Chen, F.C. Ren, Z.S. Cui, X.M. Lai, J. Iron. Steel Res. Int. **21**, 521 (2014)
48. D. Hull, D.J. Bacon, *Introduction to dislocations* (Elsevier, Oxford, 2011)

49. E.I. Galindo-Nava, J. Sietsma, P.E.J. Rivera-Díaz-del-Castillo, Acta Mater. **60**, 2615 (2012)
50. W. Roberts, B. Ahlblom, Acta Metall. **26**, 801 (1978)
51. F. Chen, Z.S. Cui, J. Liu, W. Chen, S.J. Chen, Mater. Sci. Eng. A **527**, 5539 (2010)
52. B. Derby, Acta Metall. Mater. **39**, 955 (1991)
53. H.J. Frost, M.F. Ashby, *Deformation mechanism maps: the plasticity and creep of metals and ceramics* (Pergamon Press, Oxford, UK, 1982)
54. M.S. Chen, Y.C. Lin, X.S. Ma, Mater. Sci. Eng. A **556**, 260 (2012)